PROCEEDINGS OF SPIE

Optical-turbulence characterization of a littoral test environment using a Shack-Hartmann wavefront sensor

Timothy Bukowski, Shannon O'Sullivan, Matthew Kalensky, Darren Getts, Evan Bates, et al.

SPIE.

Optical-turbulence characterization of a littoral test environment using a Shack–Hartmann wavefront sensor

Timothy J. Bukowski*[a,b], Shannon O'Sullivan[a,c], Matthew Kalensky[a], Darren Getts[a], Evan M. Bates[a], Kelsey Miller[a], and Stanislav Gordeyev[b]

[a]Integrated Engagement Systems Department, Naval Surface Warfare Center Dahlgren Division, Dahlgren, Virginia, 22448
[b]University of Notre Dame, Notre Dame, Indiana, 46556
[c]Embry-Riddle Aeronautical University, Daytona Beach, Florida, 32114

ABSTRACT

Beam propagation systems are often used in a wide range of atmospheric environments. Therefore, it is important to be able to characterize those environments in order to appropriately assess performance and inform design decisions. In this paper, a variety of methods for measuring atmospheric coherence length, r_0, were analyzed including a Shack–Hartmann-based differential image motion monitor (DIMM), gradient-tilt variance, slope discrepancy variance, and phase variance methods, as well as using the modulation transfer function (MTF). These methods were tested on varying turbulence strength environments with known atmospheric coherence lengths, first using a single modified von Kármán phase screen, then using full wave-optics simulations with 20 phase screens. The Shack–Hartmann based approaches were shown to greatly increase in error for $d/r_0 > 1$ due to discrepancies between gradient tilt and the centroid tilt measured from the SHWFS' image-plane irradiance patterns. An atmospheric data collection system was built and experimental results were taken for a beam propagating 2.4 km through a littoral environment over a 24 hour period.

1. INTRODUCTION

As a laser beam propagates through the atmosphere, phase aberrations are imposed onto the beam due to index-of-refraction fluctuations along the propagation path. These optical-turbulence environments ultimately degrade the performance of optical systems such as imaging and laser propagation systems. As such, it is desirable to quantify the atmospheric-optical-turbulence environments in which these systems operate in order to 1) predict system performance and 2) make system design decisions which appropriately account for the degradation to performance imposed by the atmosphere.[1–3] However, turbulence strength is variable and depends on location, weather, and diurnal changes, to name a few. Therefore, it is desirable to develop approaches which can easily and robustly characterize optical-turbulence strength.

In this paper, different approaches were investigated for estimating optical-turbulence strength from primarily Shack–Hartmann wavefront sensor measurements (SHWFS) but also using the far field images. These approaches were first demonstrated in simulation where the atmospheric-optical-turbulence strength was known. Complementary experimental measurements were also collected over the Potomac River Test Range (PRTR) at the Naval Surface Warfare Center Dahlgren Division (NSWCDD) in Dahlgren, VA. A previous year-long characterization of this littoral test range was conducted and the results of which are presented in Ref. 4. In this paper, we utilize different approaches for estimating optical-turbulence strength not previously used in this test environment.

As discussed above, the approaches for estimating atmospheric optical-turbulence strength presented in this paper will primarily come from measurements obtained using a SHWFS. A SHWFS is comprised of an array of subaperture lenslets focused onto a camera. Here, the average gradient of the incoming phase aberration over each subaperture in the pupil plane is estimated from irradiance-pattern deflections in the image plane.[5]

---

*Further author information:
E-mail: tbukowski@nd.edu, Telephone: (574) 631-4280

Subsequently, these so-called slope estimates are traditionally used in a least-squares reconstructor to estimate the continuous Optical-Path Difference (OPD) aberration.

There are many metrics used to quantify optical-turbulence aberrations. Here we focus on the atmospheric coherence length, also referred to as the Fried parameter, r_0.[6] Differential Image Motion Monitors (DIMM) are widely regarded as dependable instruments for measuring r_0.[7–9] The DIMM was developed in 1960 by astronomers Stock and Keller,[10] but modern implementation is described by Sarazin and Roddier.[11] The DIMM approach has been implemented using a SHWFS which works on similar principles.[12,13] In this paper, we explore using a SHWFS-based DIMM approach as well as other methods for estimating r_0 from SHWFS measurements. The other methods used in this paper include slope discrepancy variance,[14] phase variance,[15] and gradient tilt (g-tilt) variance. Brennan and Mann[16] compared the estimation error of different methods by relating the error to the number of statistically-independent degrees of freedom that each measurement technique offered. Differential image motion was shown to have the highest degrees of freedom and lowest error, which was also seen in the work presented here.

This paper is organized as follows. Section 2 describes the theory associated with each measurement approach discussed in this paper. In Sec. 3, wave-optics simulations are conducted through optical-turbulence environments of varying known r_0 values. As such, each of the approaches introduced above can be tested and compared against the known optical-turbulence strength. In Sec. 4, the system used to collect experimental measurements is introduced and the results are described in earnest. A summary and conclusions to this paper are provided in Sec. 5.

2. THEORY

With foundations in the work of Tatarskii,[17] the index-of-refraction structure constant, $C_n^2(z)$, is often used to characterize optical-turbulence strength along a path. However, with units of $m^{-2/3}$, values ranging from 1×10^{-16} to 1×10^{-12} depending on a multitude of environmental parameters, as well as strong variability along a propagation path, it is often a challenging parameter to relate to imaging and laser propagation system performance directly. Fried built on the prior developments of Kolmogorov,[18,19] Obukov,[20] and Tatarskii[17] to arrive at an atmospheric coherence length, r_0, from which it was easier to relate optical-turbulence strength to system parameters such as aperture size, D.[21,22] Here, it has been shown that r_0 elegantly describes the aperture size where ~ 1 rad^2 of phase variance is imposed onto a beam due to propagation through atmospheric turbulence. Qualitatively, when r_0 is significantly smaller than the aperture size, there will be appreciable beam spreading in the image plane. Conversely, if r_0 is larger than the aperture, the image will be close to diffraction limited. This is demonstrated using simulated data in Fig. 1. Here, a simulated beam was focused through optical-turbulence environments of increasing C_n^2. For a spherical-wave beam and uniform C_n^2 along the propagation path, it has been shown that r_0 is related to C_n^2 by[23]

$$r_0 = 3 \left(k^2 Z C_n^2 \right)^{-3/5}, \tag{1}$$

where Z is the propagation path length, and k is the wavenumber of the laser given as, $k = 2\pi/\lambda$, with λ being the wavelength of light. The resultant image-plane irradiance patterns were normalized by D/r_0 where r_0 was calculated using Eq. 1.
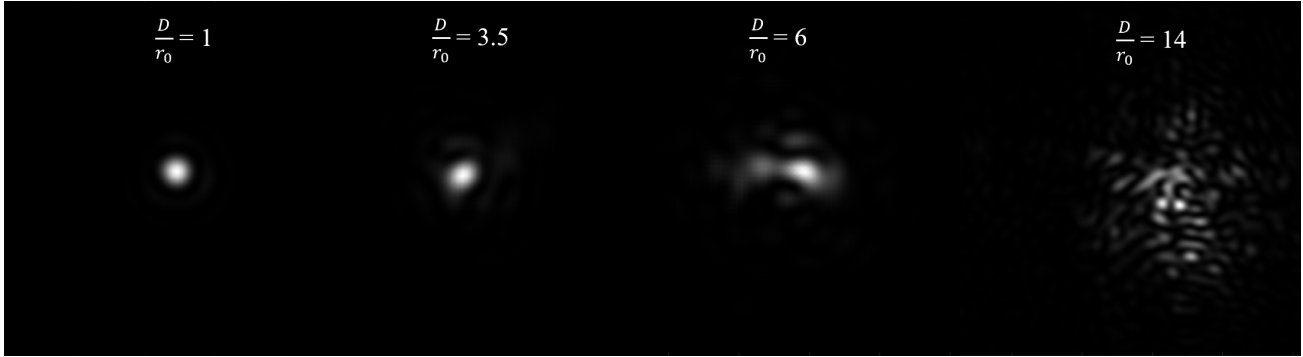
Figure 1. Image-plane irradiance patterns for 25 cm beam of wavelength 532 nm that were focused through optical-turbulence environments of increasing strength (from left to right).

Here, from the left plot of Fig. 1, we see that when $D/r_0 = 1$, the beam is essentially diffraction limited. However, as D/r_0 increases (plots from left to right in Fig. 1), we see that beam spread increases significantly. In this simulation a beam of wavelength 532nm with diameter of 25 cm was used. For the remainder of this paper, we focus on using various approaches to estimate r_0 from both simulated as well as experimental data.

2.1 Differential Image Motion Monitor (DIMM)

Many of the following methods are based on the outputs of the SHWFS which are referred to by many names including slopes, gradients, phase differences, and tilts with varying definitions. We decided to keep the equations in the form which they were derived in their respective reference, however, we took care to explicitly say which tilt definition was used. A traditional DIMM consists of two lenses of diameter, d, physically separated a distance, B. The average angle or tilt of the phase across each lens is mapped to a shifted irradiance pattern in the image-plane. These two image-plane irradiance patterns are measured on a camera from which it is trivial to calculate the image motion (or centroid motion) of the two irradiance patterns. To relate this measurement to r_0, we start with the phase structure function given as[6]

$$D_\phi(\xi, \eta) = 6.88 \left(\frac{r}{r_0}\right)^{5/3}, \tag{2}$$

where $r = \sqrt{\xi^2 + \eta^2}$ and ξ and η are the distances from a given reference point in the x and y direction, respectively. Sarazin and Roddier show that the variance of differential tilts in the longitudinal (parallel to separation), σ_l^2, and lateral, σ_t^2, directions can be related to r_0 as

$$\sigma_{l,t}^2 = K_{l,t} \left(\frac{\lambda}{d}\right)^2 \left(\frac{d}{r_0}\right)^{5/3}, \tag{3}$$

where $\sigma_{l,t}^2$ has units of $[\text{rad}]^2$, and $K_{l,t}$ is the response coefficient. This response coefficient is a function of the ratio of the lenses' separation to their diameter, $b = B/d$, where

$$K_l = 0.340(1 - 0.570b^{-1/3} - 0.040b^{-7/3}), \tag{4}$$
$$K_t = 0.340(1 - 0.855b^{-1/3} + 0.030b^{-7/3}), \tag{5}$$

as defined in Ref. 24 for g-tilt based calculations.

Using the displacements of the two measured irradiance patterns described in the beginning of this section, the image motion can be decomposed into longitudinal and lateral components, from which the differential motion can be easily computed. This method is simple as it only requires two lenses and a camera, which, along with its high fidelity r_0 measurements, has made it a standard measurement technique for estimating optical-turbulence strength.

The SHWFS operates on the same principles as a DIMM, however, instead of having two lenses, it has an array of many lenslets. The centroids calculated from the resultant image-plane irradiance patterns associated with each lenslet in conjunction with the focal length of the lenslets, allows an estimate of the gradient field to be calculated. The x and y components of these slope measurements can then be used as many different DIMM measurements. For example, a SHWFS array of 20×20 lenslet subapertures yields about 80,000 unique pairs of lenslets, each of which are used to compute r_0. These results can then be ensemble-averaged on each frame to produce r_0 estimates with low random uncertainty. In comparison, typical DIMMs yield a single measurement per frame. There are many other methods for finding r_0 using the SHWFS-measured tilts and each approach has an associated number of unique measurements which results in varying degrees of statistical accuracy. However, it has been shown that using a SHWFS as a DIMM gives the highest accuracy.[16]

2.2 Phase Variance

Another approach used for calculating r_0 is the tilt-removed phase variance, σ_ϕ^2, approach which can be computed as

$$\sigma_\phi^2 = 0.134 \left(\frac{D}{r_0}\right)^{5/3}, \tag{6}$$

where D is the aperture size.[15] As discussed in the introduction, the slope estimates obtained with the SHWFS are traditionally used in a least-squares reconstructor to estimate the continuous $OPD(x,y,t)$. After removing tip, tilt, piston, and lensing aberrations from the reconstructed $OPD(x,y,t)$ field, the OPD_{RMS} was calculated by taking the root-mean-square over the spatial dimension and temporally averaging for each data point. Subsequently, the OPD_{RMS} calculated for each data collection was used to calculate the least-squares phase variance as, $\sigma_{\phi,LS}^2 = \left[-2\pi OPD_{RMS}/\lambda\right]^2$. Here, we assume that the $\sigma_{\phi,LS}^2 \approx \sigma_\phi^2$. Under this assumption, we can use the $\sigma_{\phi,LS}^2$ calculated from the reconstructed SHWFS measurements to solve for r_0 in Eq. 6.

It is worth noting that there is also an expression relating r_0 to the tilt-included phase variance, $\sigma_{\phi,TI}^2$.[15] This expression is given as,

$$\sigma_{\phi,TI}^2 = 1.02 \left(\frac{D}{r_0}\right)^{5/3}. \tag{7}$$

However, for experimental SHWFS measurements, we recognize that turbulence-induced tip, tilt, and piston are always corrupted with mechanical contamination.[25–27] As such, it is customary to remove tip, tilt, and piston from the reconstructed $OPD(x,y,t)$ field altogether. For this reason, we opt to use the tilt-removed phase variance given in Eq. 6 instead of tilt-included phase variance given in Eq. 7.

2.3 Gradient-Tilt Variance

Since r_0 is related to the variances of optical quantities related to phase, gradient tilt (g-tilt) over an aperture can be directly related to r_0. Before proceeding, it is important to note the definition of g-tilt. G-tilt in the x-dimension over a lenslet is defined as

$$\theta_{x,g-tilt}(t) = \frac{\iint_d \nabla OPD(x,y,t) \cdot \hat{x}dxdy}{\iint_d dxdy}, \tag{8}$$

and a similar equation can be written for g-tilt in the y-dimension. The g-tilt variance, σ_{g-tilt}^2, can then be related to r_0 through[28]

$$\sigma_{g-tilt}^2 = 0.17 \left(\frac{\lambda}{d}\right)^2 \left(\frac{d}{r_0}\right)^{5/3}. \tag{9}$$

The SHWFS estimates local tilt using the centroid deflections of each lenslet's image-plane irradiance patterns along with the lenslet focal length. While we generally assume that these measurements are an accurate estimate of pupil-plane tilt, they are more suitably referred to as centroid tilt (c-tilt) as opposed to g-tilt. In strong turbulence, c-tilt becomes a poorer estimation of the desired g-tilt due to 1) non-uniform illumination,[29,30] 2) higher-order aberrations within the lenslet pupil, and 3) branch-point formation within the lenslet pupil.[31] For the purposes of this work, we assume $\sigma_{g-tilt}^2 \approx \sigma_{c-tilt}^2$. Under this assumption, each individual SHWFS subaperture irradiance pattern can be used to calculate σ_{c-tilt}^2 from which we subsequently treat as σ_{g-tilt}^2 and can then be used to estimate r_0 using Eq. 9.

2.4 Slope Discrepancy Variance

As discussed, traditionally SHWFS slope measurements are used in a least-squares reconstructor to estimate the continuous $OPD(x, y, t)$. However, in doing so, there is fitting error between the actual $OPD(x, y, t)$ field and the least-squares computed $OPD(x, y, t)$ field. Therefore, upon taking the gradient of the least-squares computed $OPD(x, y, t)$ field, these gradients will not be equal to the initially measured slopes from the SHWFS. The discrepancy between the measured slopes and the gradient of the reconstructed $OPD(x, y, t)$ field is referred to as slope discrepancy. The temporal variance of the slope discrepancy, σ_{sd}^2, can be related to r_0 by[14]

$$\sigma_{sd}^2 = \alpha \left(\frac{d}{r_0} \right)^{5/3}, \tag{10}$$

where the slope discrepancy is defined as are defined as $(\frac{\partial WF}{\partial x} - \theta_{x,g-tilt})\frac{d}{\lambda}$ and $(\frac{\partial WF}{\partial y} - \theta_{y,g-tilt})\frac{d}{\lambda}$, and α is a fitting-error parameter which depends on the experimental setup. For the work presented here, $\alpha = 0.1$.

2.5 Modulation Transfer Function

The last method used for calculating r_0 leveraged the Modulation Transfer Function (MTF), which does not come from a SHWFS, but instead from the point-spread function (PSF) of the beam. The PSF is the optical system's ability to image a point-source object. The Fourier transform of the normalized PSF yields the optical-transfer function (OTF). From this, the magnitude of the complex OTF yields the MTF. The MTF is an indication of an imaging system's ability to discern contrast by describing its proficiency in transferring different spatial frequencies from an object to an image.[32] For a given spatial frequency, a high MTF value indicates high resolution whereas a low MTF value shows blurring; i.e. it is more challenging to distinguish contrast. As r_0 gives an indication of resolution, it is natural that the MTF can be related to r_0 as shown in Ref. 32.

For a spherical wave,

$$M_{sys} = \exp\left[-4 \left(\frac{\kappa F \lambda}{D} \right)^2 \right], \tag{11}$$

$$M_{turb} = \exp\left[-4 \left(\frac{\kappa F \lambda}{D} \right)^{1/3} \left(\frac{\kappa F \lambda}{r_0} \right)^{5/3} \right], \tag{12}$$

and

$$M_{total} = M_{sys} M_{turb}, \tag{13}$$

where M_{sys} is the MTF of the optical system, M_{turb} is the MTF of turbulence-induced aberrations, M_{total} is the overall MTF, κ is spatial frequency, and F is the focal length of the imaging lens.

3. WAVE-OPTICS SIMULATION

In this section, simulations were employed to demonstrate the efficacy of the approaches described above to return the known r_0 values. First, single modified von Kármán phase screens were used. Then, full wave-optics simulations were performed. The details of which are discussed in the sections to come.

3.1 Single Phase Screen

Preliminary analysis used a simplified setup where a single phase screen was used. These phase screens were generated by filtering Gaussian white noise.[33–35] An aperture transmittance function of diameter, $D = 25$ cm, was applied to the phase screen and the resulting complex-optical field was used in a simulated SHWFS model.[5] The phase screens were created for a range of optical-turbulence conditions where C_n^2 was varied from 4×10^{-16} to 9×10^{-13} m$^{-2/3}$. The "known" r_0 values were calculated using the phase-variance approach on the finely-resolved simulation phase screen. The parameters used in simulation are in Table 1.

An example frame from the DIMM calculation using the SHWFS is presented in Fig. 2. Here, the left plot of Fig. 2 presents the r_0 results calculated from the longitudinal differential tilts and the right plot of Fig. 2 presents the r_0 results calculated from the lateral differential tils. The known r_0 value for this case was 2 mm.

Table 1. Simulation parameters

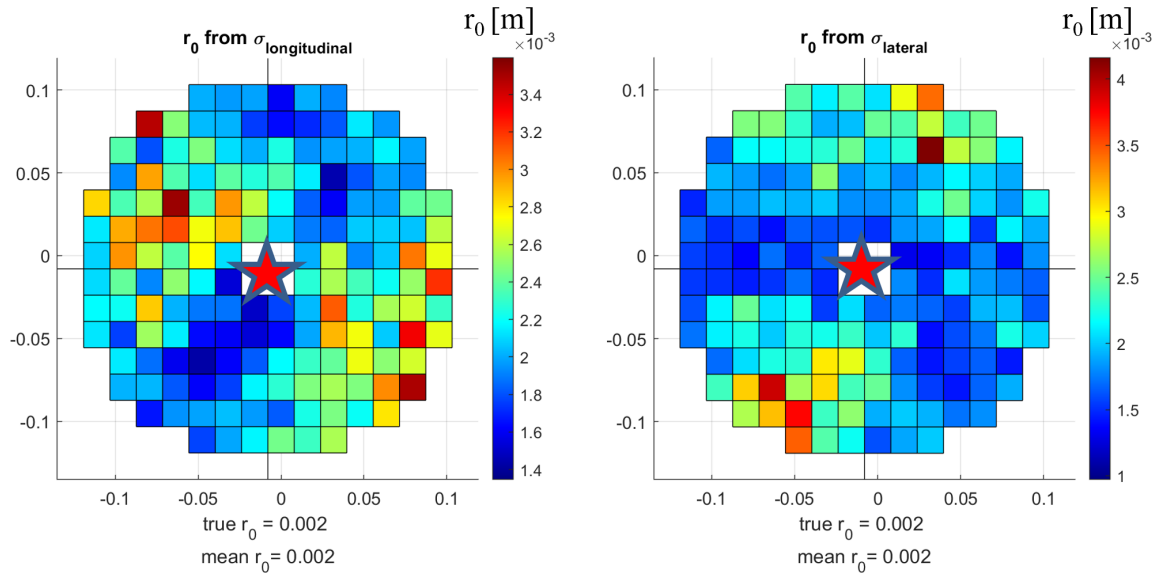| Aperture, D	25 cm
SHWFS Subaperture, d	1.6 cm
Wavelength, λ	532 nm
Path length, Z	2.4 km

Figure 2. Calculated r_0 values using the DIMM approach. Every lenslet is paired with the center lenslet highlighted with the red star. The r_0 value is shown by the colormap.

From these results, it is clear that there is variation in the calculated r_0 across the measurement pupil, highlighting the benefit of averaging over many measurements. Here, there are 197 lenslets which gives 19,306 unique lens pairs or measurements of r_0. The ratio of separation to lens diameter ranged from 1 to 16. From Fig. 2, there does not seem to be any clear preference or trend with separation distance.

Figure 3 presents the results obtained using the DIMM, phase variance, g-tilt variance, and slope discrepancy variance approaches to calculate r_0. The known r_0 values are plotted on the x-axis and the calculated r_0 values are plotted on the y-axis. The right plot of Fig. 3 presents the same results however, they are displayed on logarithmic axes. The SHWFS lenslet diameter is shown by a red dotted line. The error bars plotted for each turbulence condition denote one standard deviation calculated from 15 Monte-Carlo iterations results for each turbulence condition. Figure 4 shows the percent error of the calculated r_0 from the known r_0.
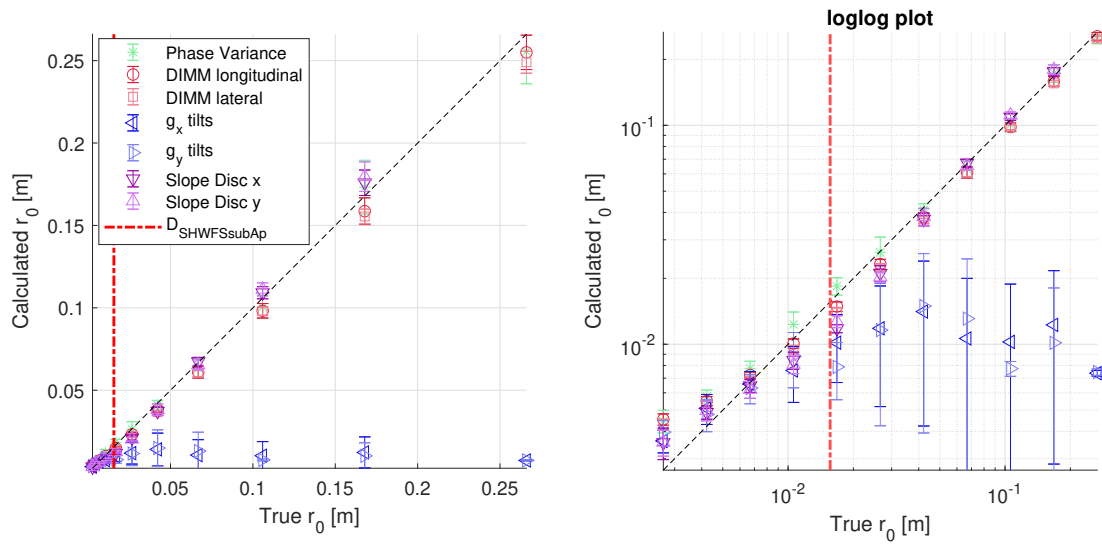
Figure 3. Results using a single phase screen. The black line denotes where the estimated or measured values equal the input or known values. Right plot shows logarithmic scale.The error bars plotted for each turbulence condition denote one standard deviation calculated from 15 Monte-Carlo iterations.
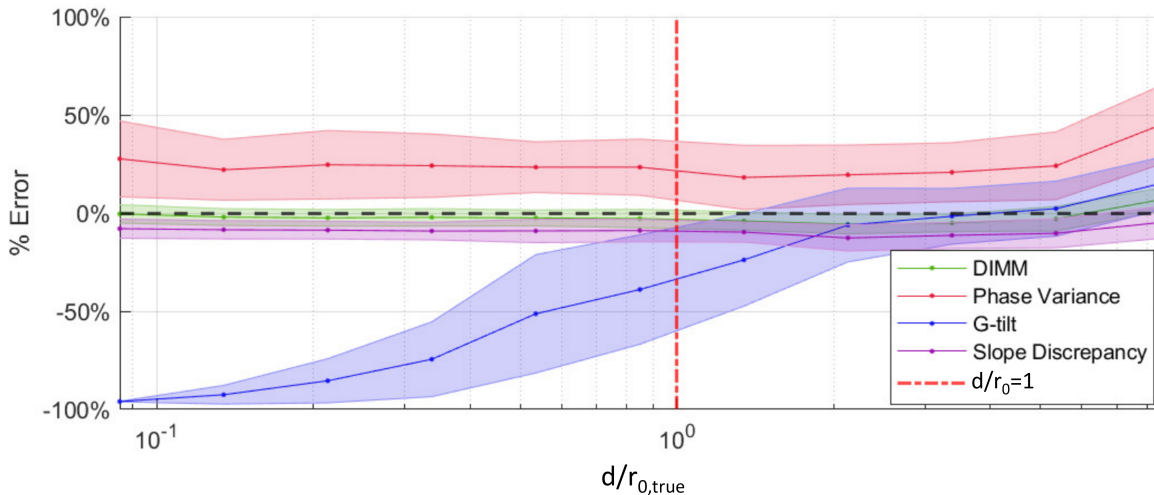

Figure 4. Single phase screen simulation percent error of calculated r_0 for each method used plotted against the ratio of the subaperture to Fried parameter d/r_0. The shaded regions denote one standard deviation from the mean.

From these two figures, we see that the lateral and longitudinal DIMM approaches both had very good agreement for the entire range of turbulence conditions explored. The phase variance approach had a consistent overestimate of r_0 by about 25%. The g-tilt variance approach in both the x and y directions tends to overestimate for $d/r_0 > 2$ and then underestimate for $d/r_0 < 2$. The DIMM, phase variance, and slope discrepancy variance approaches all have fairly consistent error for the range of turbulence strengths tested.

The shaded region in Fig. 4 signifies one standard deviation about the mean value calculated from the Monte-Carlo iterations. From these results, it can be seen that the DIMM has much lower random error as evident in the significantly smaller measurement standard deviation. Slope discrepancy variance, which is the second

highest degree of freedom SHWFS centroid-based method,[16] also has very low random error. The phase variance and g-tilt variance derived r_0 values had much more variation as demonstrated by the large shaded regions.

3.2 Full Propagation

Next, full wave-optics propagation simulations were conducted in order to capture more realistic optical-turbulence effects such as scintillation and branch-point formation. In these simulations, a point-source beacon was transmitted through phase screens via angular-spectrum propagation. The phase screens were generated by filtering Gaussian white noise[33–35] and spherical-wave angular-spectrum propagation was accomplished using the split-step beam propagation method.[33–38] After propagation, the complex-optical field was received using an aperture transmittance function and collimated. For these simulations, phase screens were created for the same range of C_n^2 values as described in Sec. 3.1. A propagation distance of 2.4 km was discretized using 20 phase screens and an aperture size of $D = 0.25$ m was imposed.

The r_0 resulting from the phase variance, DIMM, g-tilt variance, and slope discrepancy variance calculations are shown in Fig. 6 in the same format as the results presented in Fig. 3. Similar trends are observed here compared to the results from the single phase screen analysis. However, we see that in strong turbulence conditions the error increases significantly for all methods. Specifically, when r_0 becomes less than the lenslet aperture size d ($d/r_0 > 1$), we approach physical limitations of the sensor. As shown in Fig. 1, the image-plane irradiance pattern of a focused beam will spread out when $D/r_0 > 1$. All SHWFS-based methods discussed in this paper depend on the assumption that the displacement of the SHWFS irradiance patterns are proportional to the local tilt in the pupil plane. However, as described in Sec. 2.3, non-uniform illumination, branch-point formation, and appreciable higher-order aberrations will cause this assumption to break down. This leads to measured slopes that are smaller than expected, resulting in an overestimation of r_0. This has been discussed in Ref. 11. In the results presented here, the slope discrepancy variance approach underestimates r_0 for $0.4 < d/r_0 < 2.5$ before quickly rising for larger d/r_0. Similar to the results in Fig. 3, the g-tilt variance approach underestimates r_0 for low-strength turbulence.

The simulated complex-optical fields from the wave-optics simulations were also used to study the MTF approach for calculating r_0. To accomplish this, a thin-lens transmittance function was applied to the complex-optical field of the beam and angular-spectrum propagation was employed to propagate from the pupil plane to the image plane. Recall, a point-source beacon was used to conduct these simulations. As such, the resultant image-plane irradiance patterns can be treated as the PSF. The instantaneous PSF was averaged over time to achieve a long-exposure PSF and the MTF was calculated using the approach described in Sec. 2.5. Using Eqs. 11-13, an analytical MTF was created and r_0 was iterated to minimize the error of fit with the measured MTF. The fitted region of the MTF was restricted to spatial frequencies less than a cutoff frequency of the MTF. This cutoff was found by thresholding the derivative of the MTF with respect to spatial frequency at a point close to zero. The r_0 values estimated from the MTF approach are presented in Fig. 7. Here it can be seen that the MTF accurately predicts r_0 for the range of optical-turbulence conditions explored.
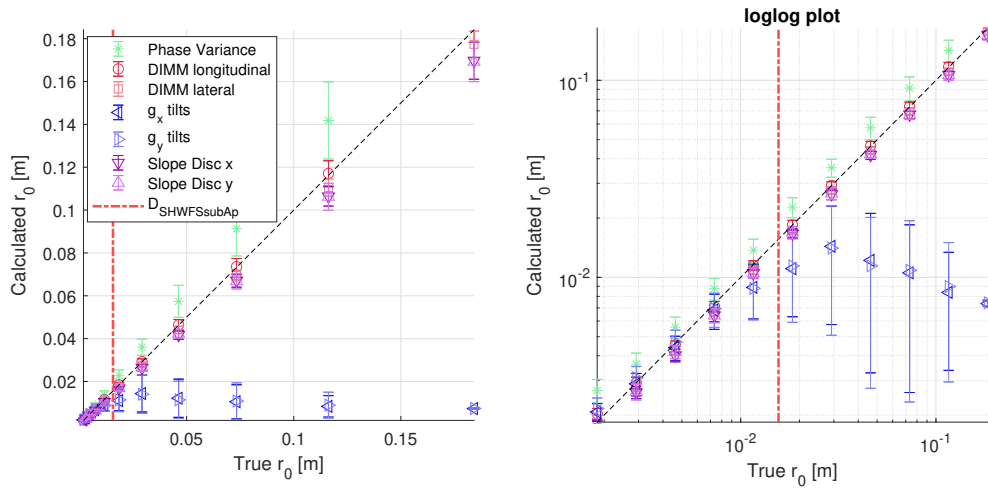
Figure 5. Results using a full wave-optics simulation. The black line denotes where the estimated or measured values equal the input or known values. Right plot shows logarithmic scale. The error bars plotted for each turbulence condition denote one standard deviation calculated from 10 Monte-Carlo iterations.
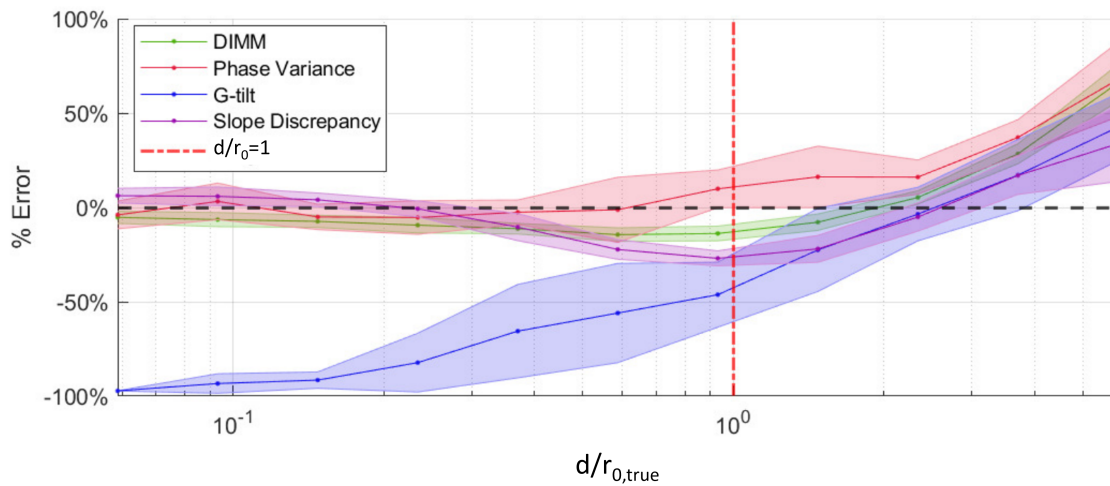

Figure 6. Percent error of calculated r_0 for each method used. The shaded regions denote one standard deviation from the mean.
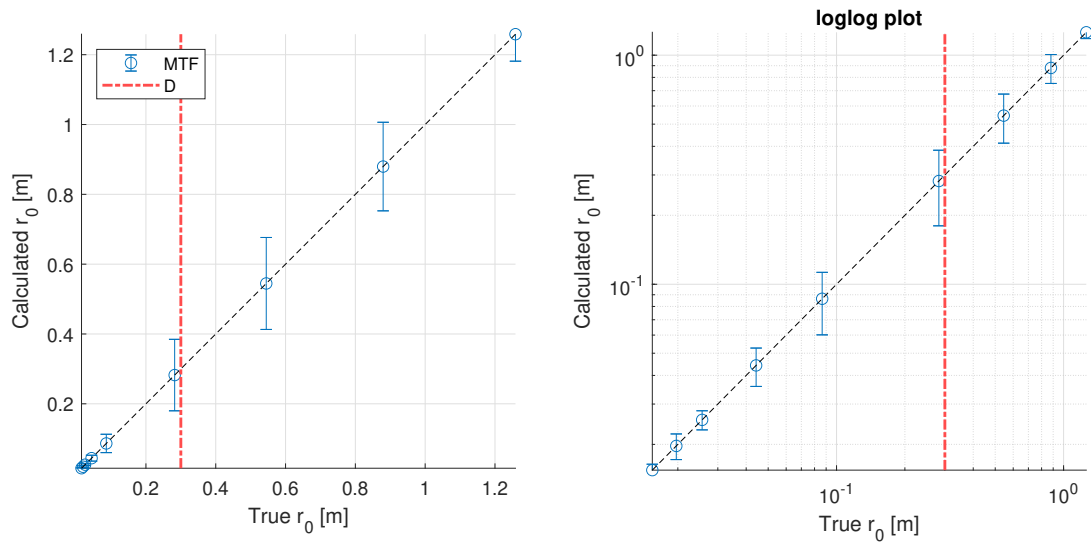
Figure 7. Results using the MTF approach for a full waveoptics simulation. The black line denotes where the estimated or measured values equal the input or known values.

4. EXPERIMENT

For these experiments, a green LED beacon (532 nm) propagated 2.4 km through a littoral test environment and was received by the data collection system. The spherical-wave beam propagated over primarily water with the last 200 m over land. The beam path is presented using a Google Earth satellite image shown in the right plot of Fig. 8. The data collection system was comprised of a 15 cm telescope with a 1500 mm focal length which collects the light from the LED beacon. Behind the telescope, a 40 mm lens was used to collimate the beam. A reimaging telescope consisting of a 175 mm followed by a 150 mm lens further reduced the beam size to approximately 3.4 mm. A beam splitter was used direct 50 % of the received signal to the SHWFS and the other 50 % to a 50 mm imaging lens which focuses the beam onto the PSF camera. The SHWFS lenslet's have a pitch of 150 μm with a focal length of 6.7 mm. Each SHWFS data point was collected at 200 Hz for 10 s with an exposure time of 7.5 ms. The PSF camera collected data at 25 Hz with an exposure time of 5 ms. Measurements were taken every 2 minutes for 24 hours. This setup, shown in the left plot of Fig. 8, is compact and fits on a 0.305 m × 0.610 m optical breadboard which was mounted to an electronically-controlled Celestron telescope mount for convenience.
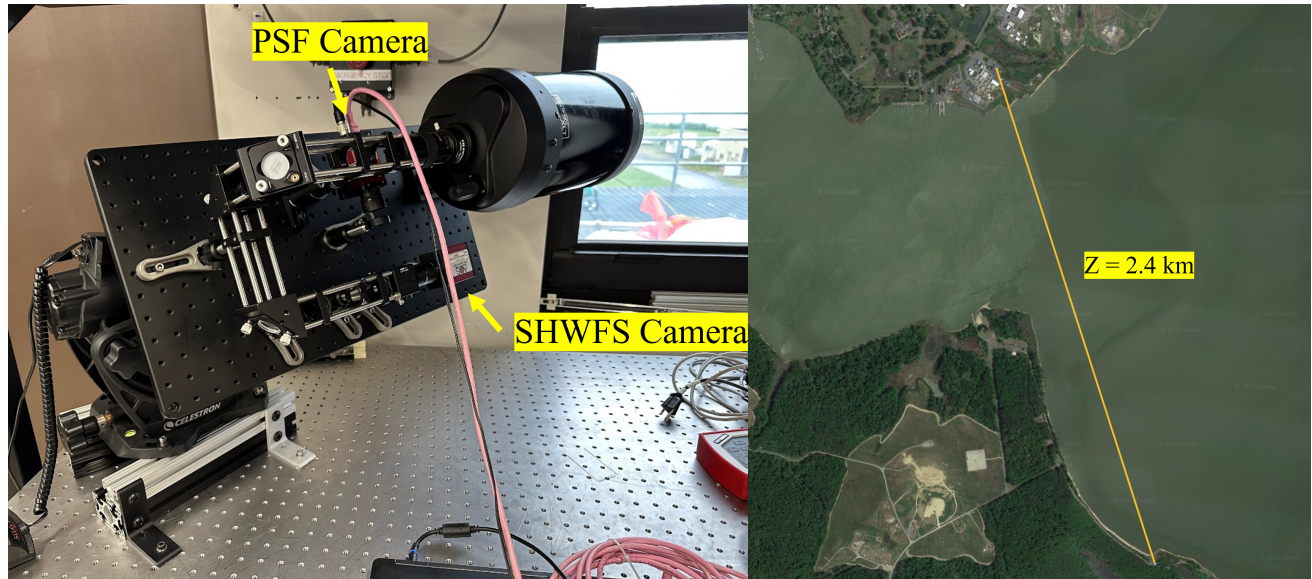
Figure 8. Experimental setup (left) and satellite view of propagation path; captured with Google Earth (right).

Example SHWFS images are shown in Fig. 9. The left image was collected before sunrise where even at this time, the irradiance variations due to scintillation are noticeable. On the right is an image which was collected in the afternoon. Here, we see that sunlight reflecting off the water began corrupting the SHWFS images. These data required additional image processing to isolate the irradiance patterns of the beacon signal before calculating centroids. Using these processed data, r_0 was calculated using the DIMM, phase variance, g-tilt variance, slope discrepancy variance. The MTF was also calculated from the PSF to estimate r_0. The r_0 values calculated using the DIMM approach are presented in Fig. 10 where the left plot presents the results for longitudinal differential tilt and the right plot presents results for lateral differential tilt. The blue stars overlayed on the plots represent the reference point from which r_0 was calculated. Similar to the results presented in Fig. 2, there is variation in the measured r_0 across the SHWFS pupil. The standard deviation between all measured subaperture pairs ranged from 5 mm to 1 mm for the large r_0 and small r_0 cases, respectively. For the smaller r_0 cases, the standard deviation was approximately equal to the mean – further highlighting the benefit of ensemble averaging results over many spatial subaperture locations.
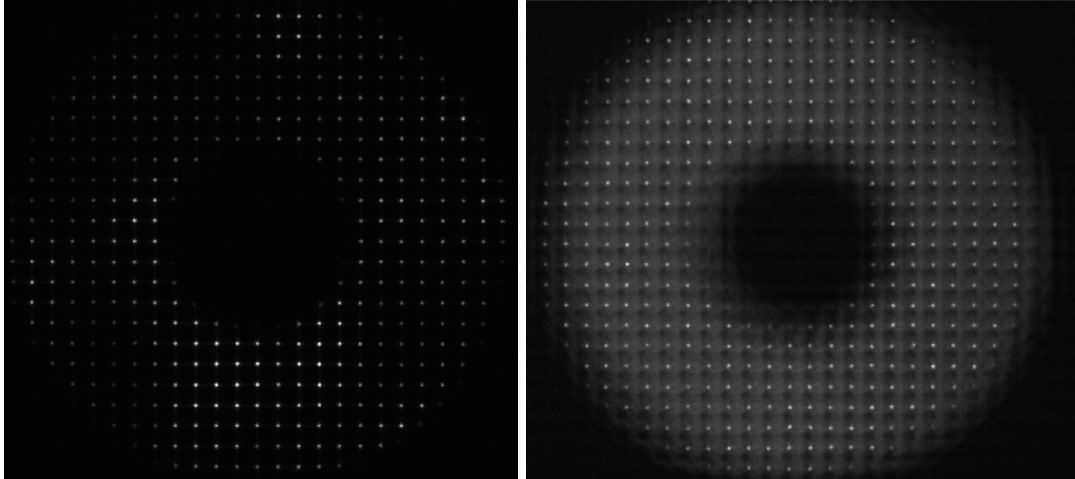
Figure 9. Example SHWFS images. (left) Good quality image from the early morning. (right) Poor quality image from midday.
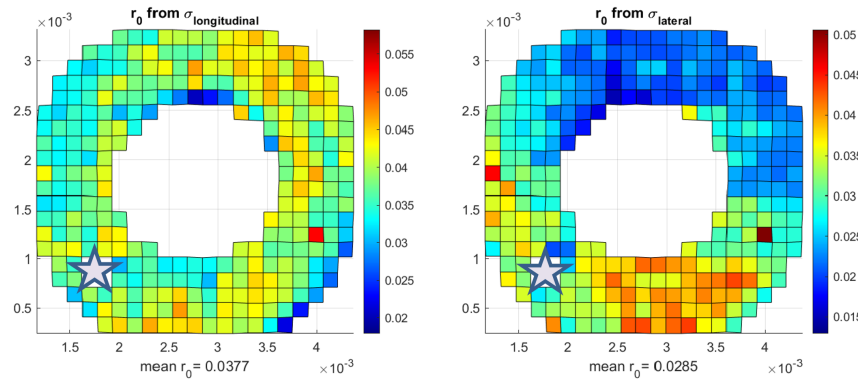

Figure 10. Calculated r_0 values using the DIMM approach. Every lenslet is paired with the center lenslet highlighted with the blue star. The r_0 value is shown by the colormap.

The measured r_0 results over a 24 hour window beginning at 5:30 am July 11, 2023 are shown in Fig. 11. By assuming that C_n^2 remained uniform along the propagation path, Eq. 1 was used to calculate corresponding C_n^2 values which are shown on the right y-axis. The longitudinal and lateral DIMM measurements were similar in magnitude and therefore, were averaged and plotted as a single line in green. The r_0 calculated from phase variance is plotted in red. The r_0 values calculated using the slope discrepancy variance in the x and y directions were also similar in magnitude and therefore, were also averaged and plotted as a single line in blue.

The SHWFS-based methods all yielded similar results. We can see that at approximately 5:30 am, r_0 starts at about 4 cm then quickly increases to over 5 cm during the neutral event at sunrise. After which, r_0 decreases to about 1 cm during the day. There is a sharp increase in r_0 to 2 cm at 2:00 pm, then it quickly returns back to about 1 cm. At the end of the day, turbulence strength begins to decrease and r_0 steadily increases through the night reaching 5 cm by 5:30 am on July 12, 2023. The results did not seem to reveal a second neutral event at sunset. The diameter of the SHWFS lenslets multiplied by the magnification of the optical system is also plotted as a horizontal dashed line in Fig. 11. Note that the r_0 during the day approaches this diameter, which will cause our measurement to overestimate r_0, as was shown in the simulation results. The d/r_0 was in the range of $0.1 < d/r_0 < 3$ which is similar to the range of values tested in the simulation.

The r_0 values calculated using the MTF approach are also plotted in orange and ranged from 0.5 - 1.5 cm which is significantly lower than the estimates obtained with the other methods. Although much stronger turbulence estimates were measured, we can see that the MTF-calculated r_0 values still follow the same trend as the other measurements. The discrepancies in the MTF results were caused by not accounting for the effects of extinction or scattering, which were likely significant. Future work is planned to measure and account for these effects to improve the accuracy of this approach.
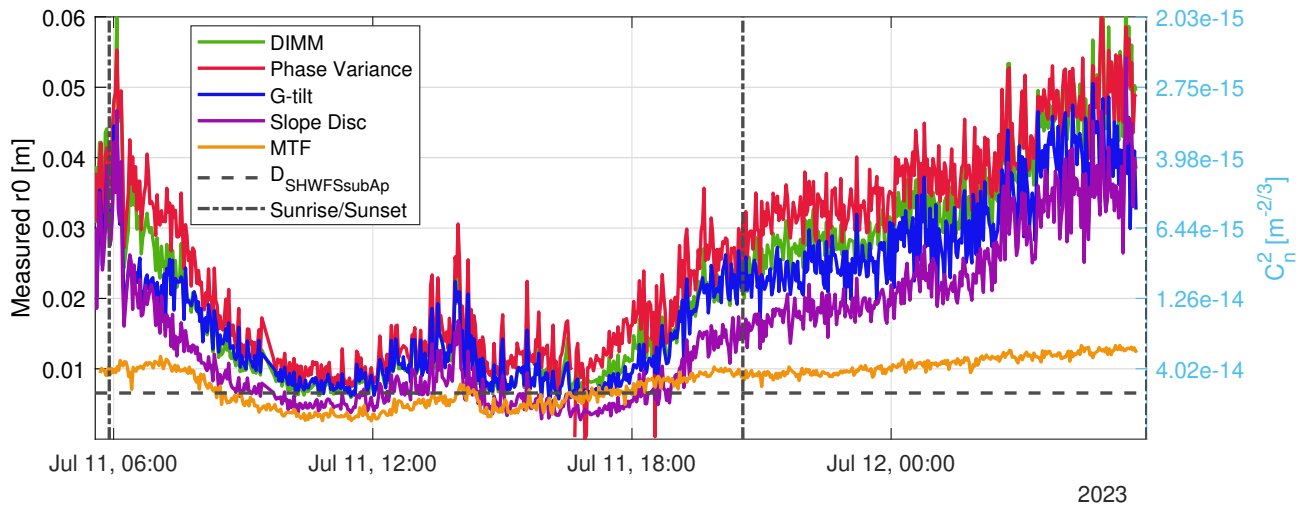

Figure 11. Measured r_0 using different methods from July 11-12, 2023.

5. CONCLUSIONS

Beam propagation systems are often used in a wide range of atmospheric environments. Therefore, it is important to be able to characterize those environments in order to appropriately assess performance and inform design decisions. In this paper, a variety of methods for measuring atmospheric coherence length, r_0, were analyzed including SHWFS-based DIMM, g-tilt variance, slope discrepancy variance, and phase variance methods, as well as using the MTF.

Using simulations, these methods were tested on varying turbulence strength environments with known atmospheric coherence lengths. First, single modified von Kármán phase screens were used, where all of the methods had consistent performance aside from the g-tilt variance approach which tended to underestimate r_0 in weak turbulence while overestimating in strong turbulence. From these results we were able to see how the DIMM approach had lower random error due to ensemble averaging over many measurements. Next, the methods were tested using full wave-optics simulations. Here it was shown that all of the SHWFS-based methods drastically increase in error when $d/r_0 > 1$. When $d/r_0 > 1$, the irradiance pattern is no longer diffraction limited and the assumption that c-tilt equals g-tilt, which is central to all SHWFS-based analysis, breaks down. This results in an underestimate of turbulence strength and overestimate of r_0.

An atmospheric data collection system was built and experimental results were taken for a beam propagating 2.4 km through a littoral environment over a 24 hour period. The SHWFS-based methods gave comparable results with r_0 around 5 cm during the night and 1 cm during the day. However, during the day, the measured r_0 values were close to the lenslet subaperture diameter, with the lowest measured r_0 having a $d/r_0 = 3$. Therefore, it is likely that these measurements resulted in an overestimate of r_0. While the MTF approach was quite accurate in simulation, the r_0 values estimated from experimental data using this approach were significantly lower than those predicted by the other approaches. This underestimation of r_0 was likely associated with not compensating for the effects of extinction and scattering. Overall, the r_0 values estimated from the simulations showed good accuracy across all methods investigated. However, to date, these simulations do not account for effects such as camera sampling/digitization, extinction, and scattering, to name a few. Therefore, further analysis is required to better understand the differences between simulation and experimental results due to the added complexities associated with empirical measurements.

Disclosures

REFERENCES

[1] Diskin, Y., Whiteley, M., Grose, M., Jackovitz, K., Drye, R., Hampshire, B., Owens, M., Smith, E., Magee, E., Kalensky, M., Jumper, E., Gordeyev, S., and Archibald, A., "Aircraft to ground profiling: Turbulence measurements and optical system performance modeling," *AIAA Journal* **59**, 4610–4625 (nov 2021).

[2] Kalensky, M., Jumper, E., Whiteley, M., Diskin, Y., Gordeyev, S., Drye, R., Archibald, A., and Grose, M., "Turbulence profiling using AAOL-BC," in [*2020 SciTech Forum*], American Institute of Aeronautics and Astronautics (jan 2020).

[3] Spencer, M. F., "Limitations of the deep-turbulence problem," in [*Imaging and Applied Optics Congress*], OSA Technical Digest (2021).

[4] Bates, E. M., Karlovich, J. Z., and Filkoski, W. L., " Year-long atmospheric characterization effort for laser weapon testing on the Potomac River Test Range at the Naval Surface Warfare Center Dahlgren Division," *Optical Engineering* **61**(7), 076105 (2022).

[5] Kalensky, M., Spencer, M. F., Jumper, E. J., and Gordeyev, S., "Estimation of atmospheric optical turbulence strength in realistic airborne environments," *Applied Optics* **61**, 6268 (jul 2022).

[6] Fried, D. L., "Optical resolution through a randomly inhomogeneous medium for very long and very short exposures," *J. Opt. Soc. Am.* **56**, 1372–1379 (Oct 1966).

[7] Tokovinin, A., "From differential image motion to seeing," *Publications of the Astronomical Society of the Pacific* **114**, 1156–1166 (Oct. 2002).

[8] Tokovinin, A. and Kornilov, V., "Accurate seeing measurements with MASS and DIMM," *Monthly Notices of the Royal Astronomical Society* **381**, 1179–1189 (10 2007).

[9] Kornilov, V., Tokovinin, A., Shatsky, N., Voziakova, O., Potanin, S., and Safonov, B., "Combined MASS–DIMM instruments for atmospheric turbulence studies," *Monthly Notices of the Royal Astronomical Society* **382**, 1268–1278 (11 2007).

[10] Stock, J. and Keller, G., "Astronomical seeing," *Stars and Stellar Systems* **1**, 138–153 (1960).

[11] Sarazin, M. and Roddier, F., "The ESO differential image motion monitor," *Astronomy and Astrophysics* **227**, 294–300 (Jan. 1990).

[12] Perera, S., Wilson, R. W., Butterley, T., Osborn, J., Farley, O. J. D., and Laidlaw, D. J., "SHIMM: a versatile seeing monitor for astronomy," *Monthly Notices of the Royal Astronomical Society* **520**, 5475–5486 (Feb. 2023).

[13] Bolbasova, L., Gritsuta, A., Lavrinov, V., Lukin, V., Selin, A., and Soin, E., "Measurements of atmospheric turbulence from image motion of laser beam by shack-hartmann wavefront sensor," in [*2019 Russian Open Conference on Radio Wave Propagation (RWP)*], IEEE (July 2019).

[14] Brennan, T. J., "Anatomy of the slope discrepancy structure function: characterization of turbulence," in [*Laser Systems Technology*], Thompson, W. E. and Merritt, P. H., eds., **5087**, 103 – 114, International Society for Optics and Photonics, SPIE (2003).

[15] Noll, R. J., "Zernike polynomials and atmospheric turbulence∗," *J. Opt. Soc. Am.* **66**, 207–211 (Mar 1976).

[16] Brennan, T. J. and Mann, D. C., "Estimation of optical turbulence characteristics from Shack Hartmann wavefront sensor measurements," in [*Advanced Wavefront Control: Methods, Devices, and Applications VIII*], Dayton, D. C., Rhoadarmer, T. A., and Sanchez, D. J., eds., **7816**, 781602, International Society for Optics and Photonics, SPIE (2010).

[17] Tatarskii, V. I., [*Wave propagation in a turbulent medium*], Dover Publications, Inc, Mineola, New York (2016).

[18] Kolmogorov, A., "Dissipation of energy in the locally isotropic turbulence," *Proceedings of the Royal Society* **434**, 15–17 (jul 1991).

[19] Kolmogorov, A., "The local structure of turbulence in incompressible viscous fluid for very large reynolds numbers," *Proceedings of the Royal Society* **434**, 9–13 (jul 1991).

[20] Obukhov, A., "Structure of temperature field in turbulent flow," tech. rep., Air Force Systems Command (1970).

[21] Fried, D., "Optical heterodyne detection of an atmospherically distorted signal wave front," *IEEE* **55**(1), 57–77 (1967).

[22] Fried, D. L., "Limiting resolution looking down through the atmosphere," *Journal of the Optical Society of America* **56**, 1380 (oct 1966).

[23] Tyson, R. K., [*Principles of Adaptive Optics, Second Edition*], Academic Press, hardcover ed. (10 1997).

[24] Conan, R., Borgnino, J., Ziad, A., and Martin, F., "Analytical solution for the covariance and for the decorrelation time of the angle of arrival of a wave front corrugated by atmospheric turbulence," *J. Opt. Soc. Am. A* **17**, 1807–1818 (Oct 2000).

[25] Kalensky, M., *Airborne Measurement of Atmospheric-Induced Beam Jitter*, PhD thesis, University of Notre Dame (2022).

[26] Kalensky, M., Jumper, E. J., Kemnetz, M. R., and Gordeyev, S., "In-flight measurement of atmospheric-imposed tilt: experimental results and analysis," *Applied Optics* **61**, 4874 (may 2022).

[27] Kemnetz, M. R. and Gordeyev, S., "Analysis of aero-optical jitter in convective turbulent flows using stitching method," *AIAA Journal* , 1–17 (sep 2021).

[28] Tyler, G. A., "Bandwidth considerations for tracking through turbulence," *Journal of the Optical Society of America A* **11**, 358 (Jan. 1994).

[29] Barchers, J. D., Fried, D. L., and Link, D. J., "Evaluation of the performance of hartmann sensors in strong scintillation," *Applied Optics* **41**, 1012 (feb 2002).

[30] Holmes, R. B., "Scintillation-induced jitter of projected light with centroid trackers," *Journal of the Optical Society of America A* **26**, 313 (jan 2009).

[31] Kalensky, M., "Branch-point identification using second-moment shack–hartmann wavefront sensor statistics," *Applied Optics* **62** (May 2023).

[32] Andrews, L. C. and Phillips, R. L., "Imaging systems analysis," in [*Laser Beam Propagation through Random Media*], ch. 14, 607–643, SPIE, 2nd ed. (2005).

[33] Schmidt, J., [*Numerical simulation of optical wave propagation with examples in MATLAB*], SPIE, Bellingham, Wash (2010).

[34] Martin, J. M. and Flatté, S. M., "Intensity images and statistics from numerical simulation of wave propagation in 3-d random media," *Applied Optics* **27**, 2111 (jun 1988).

[35] Martin, J. M. and Flatté, S. M., "Simulation of point-source scintillation through three-dimensional random media," *Journal of the Optical Society of America* **7**, 838 (may 1990).

[36] Knepp, D., "Multiple phase-screen calculation of the temporal behavior of stochastic waves," *IEEE* **71**(6), 722–737 (1983).

[37] MACASKILL, C. and EWART, T. E., "Computer simulation of two-dimensional random wave propagation," *IMA Journal of Applied Mathematics* **33**(1), 1–15 (1984).

[38] Roggemann, M., [*Imaging through turbulence*], CRC Press, Boca Raton (1996).